Materials Science

Research article

Effect of the incorporation of BiFeO$_3$ on the structural, electrical and magnetic properties of the lead-free Bi$_{0.5}$Na$_{0.5}$TiO$_3$

Pablo Wolfgang Zúñiga-Mera[1], Sonia Gaona Jurado[1], Alejandra Isabel Guerrero Duymovic[1], Claudia Fernanda Villaquirán Raigoza[1,]* and José Eduardo García[2]

[1] Department of Physics, Science and Technology of Ceramic Materials Group (CYTEMAC), University of Cauca, Popayan, Colombia

[2] Department of Applied Physics, Polytechnic University of Catalunya, c/Jordi Girona 1-3, B4, 08034, Barcelona, Spain

* **Correspondence:** Email: gure@unicauca.edu.co; Tel: +57-2-8209800.

Abstract: Powders of the system $(1–x)$Bi$_{0.5}$Na$_{0.5}$TiO$_3$–xBiFeO$_3$ (x = 0, 0.02, 0.08, 0.10) are synthesized by the combustion reaction method. The crystal structure and the particle size of Bi$_{0.5}$Na$_{0.5}$TiO$_3$ are modified by the incorporation of BiFeO$_3$, as can be seen from the infrared spectroscopy and X-ray diffraction results. The inclusion of iron and the increase in the molar percentage of bismuth in the BNT matrix generate new bonds with a different force constant. The structural analysis showed that the addition of BFO to the BNT does not induce any structural phase transition, preserving the rhombohedral symmetry of the Bi$_{0.5}$Na$_{0.5}$TiO$_3$ system. The electrical measurements show that the incorporation of iron increases the conductivity of the system generated by an increase in the concentration of oxygen vacancies; alternatively, the addition of 10% of BiFeO$_3$ generates ferrimagnetic behavior reflected in the magnetic hysteresis curves obtained at room temperature.

1. Introduction

One of the promising approaches to create new materials is the combination of different physical properties in a material to increase its functionality. The coupling between the parameters of magnetic and ferroelectric order can lead to magnetoelectric effects, in which magnetization may

occur by means of the application of an electric field and vice versa. As to the date, not many multiferroic materials have been identified, and for those that are known, the mechanism underlying their ferroelectricity is often unconventional [1]. The bismuth and sodium titanate, $Bi_{0.5}Na_{0.5}TiO_3$ (BNT) with rhombohedral perovskite structure distorted at room temperature is considered an excellent lead-free ferroelectric material, because has a large remaining polarization of 38 $\mu C/cm^2$, and Curie temperature of 320 °C; some authors have reported phase coexistence at 200 °C [2,3], but the existence of phase coexistence is an open question [4]. The BNT has a high coercive field of 73 kV/cm, and its relatively high conductivity, makes it difficult to polarize [5].

On the other hand, $BiFeO_3$ is a widely used multiferroic compound because its electric and magnetic transition temperatures are above the room temperature ($T_C \sim$ 820–850 °C, T_N = 370 °C) being an excellent candidate for the development of multiple applications [6]. One of the biggest problems with this compound is the presence of impurities that increase the electrical conductivity. High electrical conductivity can mask the phenomenon of ferroelectricity. According to the above, more attention has been focused on introducing substitutions to enhance magnetization [7,8], improve the insulating and piezoelectric properties [9], among others.

Both $Bi_{0.5}Na_{0.5}TiO_3$ (BNT) and $BiFeO_3$ (BFO) have a perovskite structure with a spatial group R3c at room temperature. When mixed, it is formed a BNT–BFO solid solution with more structural stability. It has been shown that BNT–xBFO solid solution for x = 0, 0.2, 0.5, 0.7 has a spatial group R3c at room temperature [10]. The system has a ferroelectric behavior for all studied compositions of the solid solution and two different domains of dielectric properties are distinguished [10]. Recent studies in thin films of BNT–xBFO for x $\leq$ 0.20, showed that the films exhibit a ferroelectric behavior and magnetic properties comparable to that of $BiFeO_3$ [11]. For $0.7BiFeO_3$–$0.3Bi_{0.5}Na_{0.5}TiO_3$ thin films it was found potential ferroelectric properties at low temperatures and improved insulating resistance [12].

Furthermore, it is well known that the physical, chemical and mechanical properties of a ceramic material are largely dependent on the quality of the starting powders (particle size, morphology, etc.). In order to obtain high quality ceramics powders and improve their functionality, different synthesis methods have been employed. BNT ceramic powders have been obtained by solid-state reaction [13], sol-gel [14], hydrothermal method [15], and mechanochemical [16] methods. The combustion synthesis (CS) is a good alternative to achieve a rapid and energy-efficient synthesis. A typical CS procedure uses a self-sustained exothermic reaction among well-mixed reactants to achieve a rapid and low-cost synthesis of particulate products. The main characteristic of this process is that the heat required to conduct the reaction is supplied by the reaction itself and not from an external source [17]. According to the above, the aim of this work is to improve functionality of electric and magnetic properties of BNT ceramics with substitution of low concentration of BFO using a low cost fabrication method. We present the influence of BFO on the structural, electrical and magnetic properties of BNT, in the system (BNT–xBFO) for x = 0, 0.05, 0.08, 0.10, 0.20 obtained by the combustion reaction method.

2. Materials and methods

Bismuth nitrate ($Bi(NO_3)_3$ RA-Chemicals-98%), sodium nitrate ($Na(NO_3)_3$ Aldrich-98%), titanium tetrabutoxide (TBT Across-99%) and iron nitrate ($Fe(NO_3)_3$ Aldrich-97%) were used for the synthesis of the BNT–xBFO system (x = 0, 0.05, 0.08, 0.10, 0.20). Urea (CON_2H_4 Merck-99.5%)

and glycine ($C_2H_5NO_2$ Merck-98%) were used as fuels in a 50:50 ratio. First, each precursor was dissolved in water and/or nitric acid (HNO_3), until obtaining a transparent solution that indicates the non-formation of precipitates; also, the fuels were diluted in water until dissolution. The resultant solution was then evaporated and dried at approximately 200 °C on a hot plate under continuous stirring at ~300 rpm until the majority of the solvent is removed. This mixture was then heated in muffle furnace at a temperature of 600 °C. Evaporation occurs which is followed by combustion. The resultant product consists of foamy flakes which are macerated in an agate mortar and the obtained powder is then calcined at a temperature of 800 °C for 4 h; in the Figure 1 we show a schema of the synthesis method.
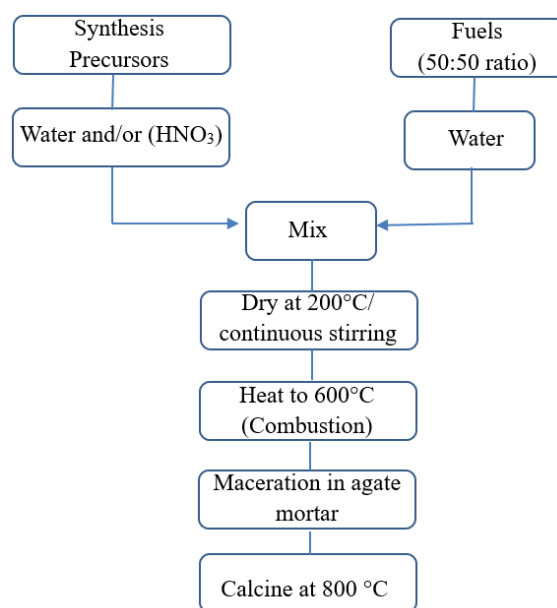
Figure 1. A schematic figure for the synthesis of the obtained materials.

The ceramic powders were characterized by infrared spectroscopy with fourier transform using a SHIMADZU IR Affinity-FT infrared Spectrophotometer 4000–225 cm^{-1}. For the qualitative and semi quantitative analysis, the deconvolution of the bands took place using the Fityk 0.9.2 software [18]. The phase formation was investigated by X-ray diffraction (X'pert PRO PANalytical) equipped with Cu Kα (λ = 1.5418 Å) a wide range of Bragg angles 2θ (20°–80°) at scanning rate of 0.02° per minute. GSAS program [19] was used to analyze the phases in the diffractogram and to know their crystallographic characteristics. A vibrating sample magnetometer (VSM, the Quantum Design VersaLab Instrument) was used for magnetization measurements as a function of the magnetic field. X-ray profile analysis is a simple and powerful tool for estimating crystallite size and lattice deformation [20–22]. The Williamson–Hall analysis (W–H) is a simple method where the deconvolution of the diffraction profile width is induced by both the size of the crystallite and the deformation, considering the peak width as a function of 2θ [23]. In this study, the W–H analysis was used to estimate the crystallite size and the deformation of the lattice. The ceramic powders were processed by the slip casting method to obtain green ceramic pieces that were subsequently sintered. The ceramic processing may undergo three stages: obtaining the slip, obtaining the pellets, and sintering. To obtain the slip, it was necessary to perform the calculation of solids and liquids from Eq 1

that relates the densities and concentrations of BNT, distilled water and the optimum density of the slip containing the oxide. Substituting the respective values in Eq 1, Eq 2 is obtained. From the calculations, taking into account that the total concentration must be equal to 1 (Eq 3), we obtain the quantity of solids and liquids necessary to stabilize the particles in suspension in the presence of a deflocculant, as seen in Eqs 4 and 5. In this process, a change occurs in the surface electrical charge of the particles, causing an increase in the repulsive forces avoiding the attraction between them [24]. Literature reports an ideal density value of 2.1 g/cm^3 [25] to guarantee a stable slip containing an oxide.

$$\frac{1}{2.1\frac{g}{cm^3}} = \frac{[H_2O]}{theoretical\ density\ of\ water} + \frac{[BNT]}{BNT\ density} \tag{1}$$

$$\frac{1}{2.1\frac{g}{cm^3}} = \frac{[H_2O]}{1\frac{g}{cm^3}} + \frac{[BNT]}{5.99\frac{g}{cm^3}} \tag{2}$$

$$1 = [H_2O] + [BNT] \tag{3}$$

$$2.85 = 5.99 - 5.99[BNT] + [BNT] \tag{4}$$

$$62.9\% = [BNT] \tag{5}$$

Pellets of 10 mm diameter were prepared by slip casting. An appropriate amount of slip is deposited in a mold and is left at rest for 3 h, where it acquires enough mechanical resistance to remove them from the mold. The highest density was obtained by sintering the pellets at 1120 °C for 2 h, finding a density of 5.81 g/cm^3 (96% of the theoretical density). The two circle surfaces of sintered ceramics were polished, coated with silver paster as the electrode and fired at 500 °C for 30 min. The dielectric properties measures were achieved with an impedance gain/phase analyzer SI 1260 (Solartron Analytical).

3. Results and discussion

Figure 2 shows the FTIR spectra of ceramic powders of the BNT–xBFO system. Three regions can be distinguished in the spectra: (i) a band located around 3500 cm^{-1} (R1) associated to the mode of flexion of the water molecule of the environment; (ii) between 1300 and 1700 cm^{-1} (R2) bands associated with vibrational modes of adsorbed C–O, of the CO_2 of air [26]; (iii) between 1100 and 470 cm^{-1} (R3), there are bands corresponding to functional groups associated with metal-oxygen bonds and may point to the BNT–xBFO system formation.

The spectra in R3 interval was analyzed in more detail by means of the deconvolution process (Figure 3). Figure 3a shows the deconvolution of the spectrum corresponding to the pure BNT sample where bands related to the Ti–O bond within the [TiO_6] octahedron are at 560, 585 and 637 cm^{-1}; these bands are characteristics of the formation of perovskite [27,28]. There is also a band around ~862 cm^{-1} that belongs to the Bi–O bond [29] and a band around ~769 cm^{-1} that is associated with the stretching mode of the Bi–O bond in [BiO_3] [30,31]. The vibrational modes of Na_2O are below 400 cm^{-1}, so characterization by Raman spectroscopy is required to identify this functional group. For $x = 0.05$ (Figure 3b), the shift to a greater wave number of the bands belonging to the Ti–O bond is evident. The bands belonging to the Bi–O bond undergo a displacement at ~785 cm^{-1} and ~852 cm^{-1}.

Additionally, three new bands appear: one around ~526 cm^{-1} associated with the Bi–O bond within the BiO$_6$ [32] octahedron; a second band at ~546 cm^{-1} that belongs to the stretching mode of the Fe–O bond in the octahedral FeO$_6$ [32] and a third band around ~727 cm^{-1} corresponding to the stretching mode of the Bi–O bond in BiO$_3$ [30,31].
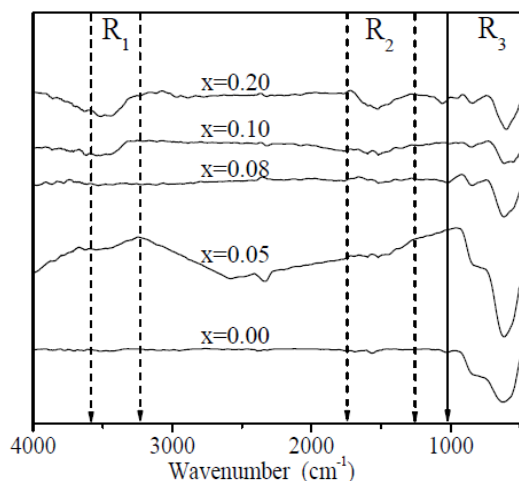
Figure 2. Infrared spectra of ceramic powders of the BNT–xBFO system.
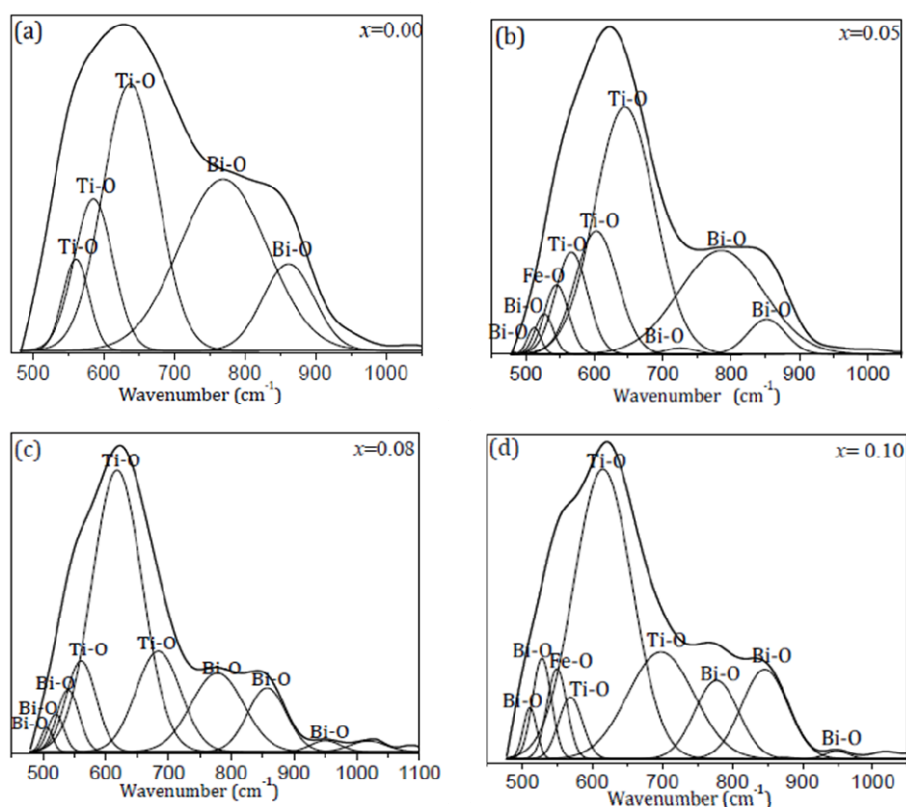
**Figure 3.** Deconvolution of the IR spectrum of ceramic powder of the BNT–xBFO system between 470 and 1100 cm^{-1} for: (a) x = 0.00, (b) x = 0.05, (c) x = 0.08 and (d) x = 0.10.

For x = 0.08 (Figure 3c), the bands associated with the vibrations of the TiO_6 octahedron move to ~561 cm^{-1}, ~618 cm^{-1} and ~684 cm^{-1} while the bands of the Bi-O bonds undergo a displacement towards ~778 cm^{-1}, ~857 cm^{-1}. Furthermore, there are two new bands: one around ~506 cm^{-1} associated with the twisting mode of the Bi-O bond in the bismuthate group (BiO_3) [33] and another one ~949 cm^{-1} related to the stretching mode of the Bi–O [34]. For x = 0.10, the bands do not experience a significant change (Figure 3d).

When BFO is incorporated into the structure of the BNT, the Fe occupies the site of the Ti since the ionic radii of Fe is closer to the ionic radii of Ti (r_{Fe}^{3+} = 0.65 Å, r_{Ti}^{4+} = 0.61 Å, both in coordination 6 [35]) than the radii of Bi and Na (r_{Bi}^{3+} ~ 1.38 Å, r_{Na}^{1+} = 1.39 Å, both in coordination 12 [36]). Increasing the concentration of BFO, the displacement of the bands may be due to: (i) the variation in the electronegativity difference of the new bonds, which is proportional to the strength of the bond, an indirect measure of the resistance of the molecule to be deformed [37]. For example, the Ti–O bond has an electronegativity difference of 2.0, that is greater than that of the Fe–O bond (1.7), which makes the vibration frequencies of the TiO_6 octahedra different; (ii) the incorporation of BFO makes the percentage of bismuth higher than that of Na, while iron ions are incorporated in the titanium sites; the difference of atomic masses between Bi (208.98 g/mol), Na (22.98 g/mol), Ti (47.90 g/mol) and Fe (55.84 g/mol) causes a change in the frequency of vibration, related to the reduced mass of the system by the relation $\nu = \sqrt{\dfrac{k}{\mu}}$, where k is the force constant of the bonds and μ the reduced mass.

Figure 4 shows the X-ray diffraction patterns. For x = 0, it is observed that the system crystallizes in a major phase related to the $Bi_{0.5}Na_{0.5}TiO_3$ system, with rhombohedral symmetry with space group R3c at room temperature and lattice parameters a = b = 5.4902 Å and c = 13.4859 Å, according to the CIF (Crystallographic Information File) number 2103295 [38,39]. In all the diffractograms, it is observed, that the majority crystalline phase corresponds to the perovskite structure of the $Bi_{0.5}Na_{0.5}TiO_3$ system. In general, the addition of BFO to the BNT does not induce any structural phase transition, preserving the rhombohedral symmetry, in agreement with previously reported results [40].
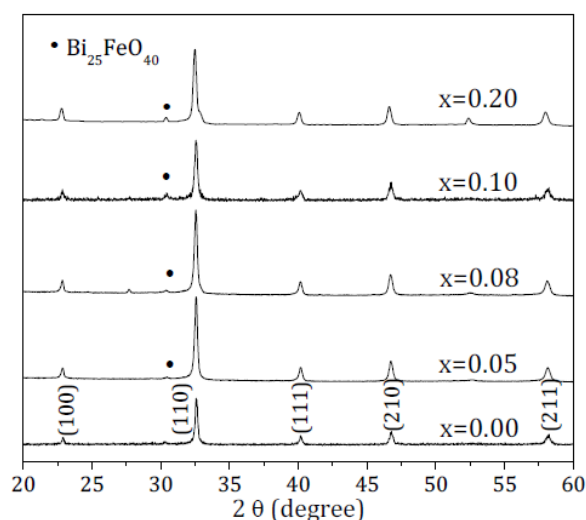
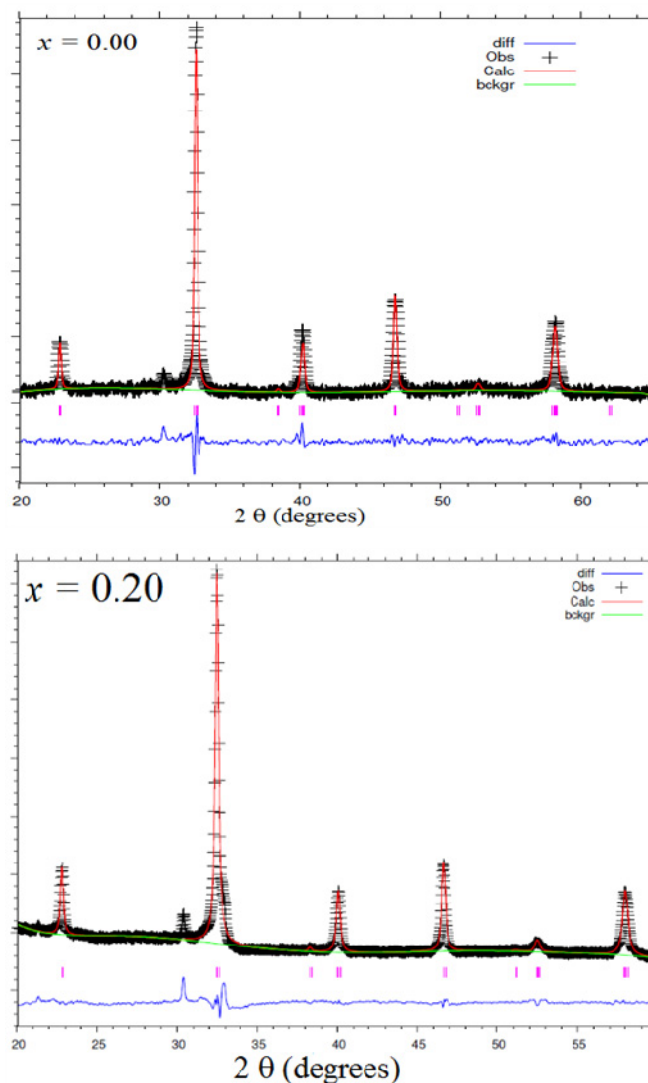**Figure 4.** X-ray diffractograms of BNT–xBFO ceramic powders.

The Goldschmidt tolerance factor t is an indicator of the stability and distortion of the perovskite structure ABO_3 [41], allowing to predict the symmetry of the structure based on the ratio of the ionic radius, $t = \frac{R_A + R_O}{\sqrt{2}(R_B + R_O)}$ where R_A, R_B and R_O are the ionic radii of the cations A, B and oxygen, respectively. For t = 1 the symmetry is cubic. When t decreases the structure becomes distorted; values of t < 1 imply the compression of the B–O bonds and the elongation of the A–O bonds: the structure tends to twist the octahedrons to relieve the tensions caused by the mismatch in the sizes of the cations. When t > 1, the opposite occurs, the B–O bonds are lengthened and the A–O bonds are compressed and the hexagonal symmetry is stabilized [42,43]. The tolerance factor calculated for the BNT is t ~ 0.98 indicating that it is a distorted perovskite, in agreement with the values reported in the literature [44,45].

The Figure 5 shows the behavior of t for the different compositions of the BNT–xBFO system, it is observed that the tolerance factor decreases with the increase of x, due to a structural distortion. A detail analysis of the diffractograms by means of the program GSAS helped us to confirm this hypothesis.
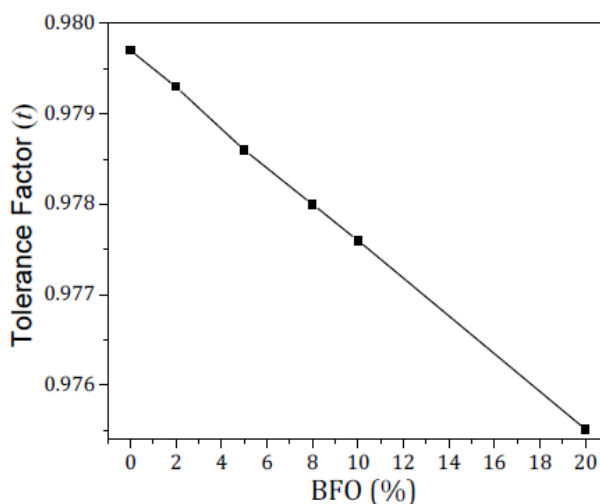
**Figure 5.** Tolerance factor for the BNT–xBFO solid solution.

The XRD patterns of the sample were analyzed by employing the Rietveld refinement method with the help of GSAS software. The Table 1 shows the lattice parameters, volume, crystallite size and deformation obtained from the Rietveld refinement for all compositions studied, and in the Figure 6 are shown two XRD spectra and Rietveld analysis, (x = 0.00, 0.20). It is seen that the volume of the cell increases due to the increase of the lattice parameters with the increase of BFO, as reported in the literature [46].

Figure 6. Rietveld refinement of the diffractograms of BNT–xBFO using the GSAS program, for values of x = 0.0 and 0.20.

The evolution of the lattice parameters as a function of the composition x, are shown in Figure 7. The lattice distortion can be due to: (i) the difference of ionic radii of the cations occupying the B site in the perovskite structure (r_{Fe}^{3+} = 0.65 Å, r_{Ti}^{4+} = 0.61 Å), while the radius difference of the cations occupying site A is not representative (r_{Bi}^{3+} = 1.38 Å, r_{Na}^{1+} = 1.39 Å) [47]; (ii) the valence difference that generates vacancies and can be represented by $Bi_{0.5}Na_{0.5}TiO_3 \xrightarrow{BiFeO_3} Bi_{Bi}^{\times} + 2Fe_{Ti}' + V_O^{\bullet\bullet}$ and (iii) the difference in electronegativity that determines the percentage of covalence and/or ionicity, which affects the length of the bonds that are part of the crystal structure. For most fittings, except for x = 0.08, low values of χ^2 (<2) are obtained, signaling a good refinement.
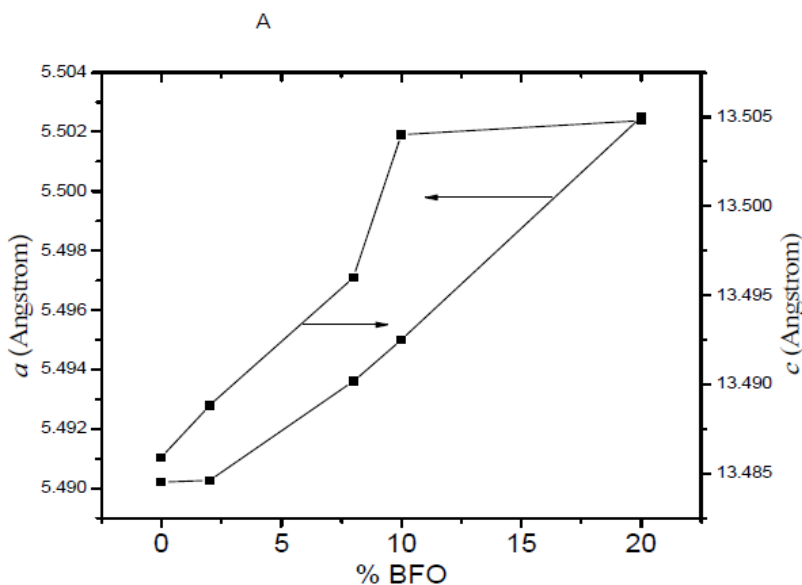
Figure 7. Variation of the parameters a and c for the different values of x of the BNT–xBFO system.

Generally, changes in the microstructure of a sample affect the intensity and the width of the X-ray diffraction peaks. Improving the Scherrer formalism, Williamson and Hall identified that the grain size and lattice strain are two main sources of X-ray diffraction peak broadening at certain room temperature [48]. According to Scherrer's method for the size of nanoparticles, the Scherrer's crystalline size, D, is given by the Eq 6 [49]:

$$D = \frac{K\lambda}{\beta_D \cos\theta} \tag{6}$$

where K is the shape factor (0.9), β_D is the peak width due to the crystallite size, λ is the wavelength of Cu-k$_\alpha$ radiation and θ is the diffraction angle. In order to understand the peak broadening with lattice strains, various peaks in the XRD pattern were used. The Stokes and Wilson formula given in Eq 7 was used to calculate the strain induced broadening of the Bragg's diffraction peak [50]:

$$\varepsilon = \frac{\beta_{hkl}}{4\tan\theta} \tag{7}$$

One can rewrite Eq 6 as Eq 8:

$$\beta_{hkl}\cos\theta = \left(\frac{k\lambda}{D}\right) + 4\varepsilon\sin\theta \tag{8}$$

where β_{hkl} is the total width at the average intensity (FWHM) [51,52].

A plot of $4\sin\theta$ and $\beta_{hkl}\cos\theta$ is shown in Figure 8. Using a linear fit to the data, the crystalline size was estimated from the y-intercept, and the strain ε, from the slope of the fit. Eq 8 represents the uniform deformation model considering the isotropic nature of the crystal, where the strain was assumed to be uniform in all crystallographic directions. The Table 1 shows the values of ε and D for each concentration. When the BFO concentration increases, the crystallite size increases from 43.08 nm (x = 0) to 139.19 nm (x = 0.20), ε also increases from 0.01 for x = 0 to 0.09 for x = 0.20.
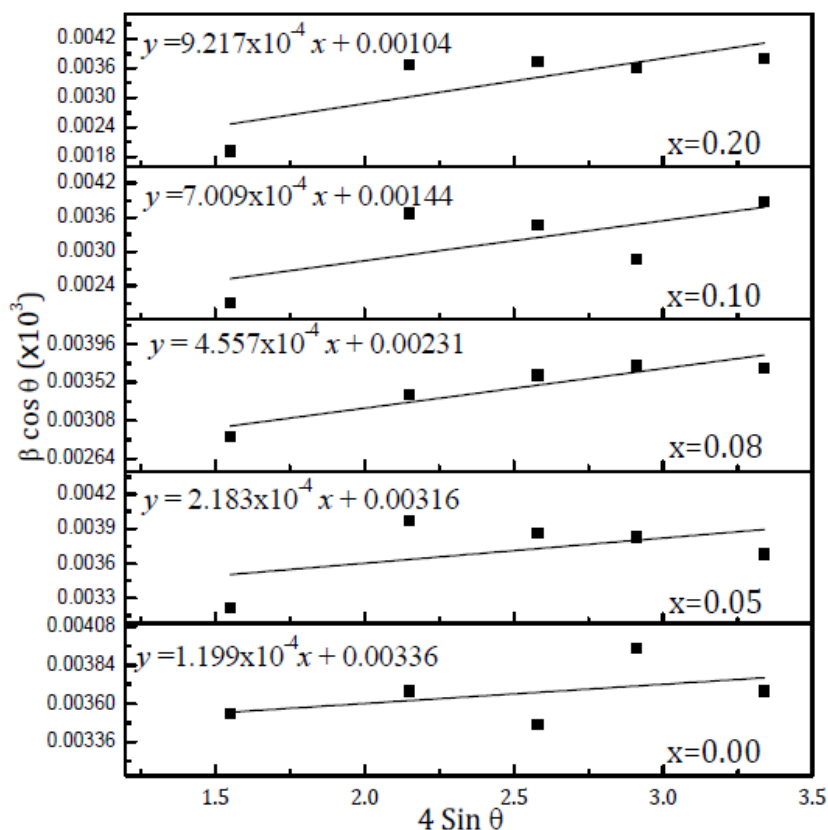
Figure 8. Variation of $\beta cos\theta$ vs $4sin\theta$ for different concentrations.

Table 1. Lattice parameters, volume, lattice strain and crystallite size obtained from the Rietveld refinement adjustment of the system $(1-x)Bi_{0.5}Na_{0.5}TiO_3-xBiFeO_3$ using the GSAS program.

| x	Lattice parameters		Volume (Å)^3	χ^2	W–H	
	$a = b$ (Å)	c (Å)			$\varepsilon\%$	D (nm)
0.00	5.4902	13.4859	352.039	0.26	0.0119	43.08
0.02	5.4902	13.4888	352.121	2.00	0.0218	45.81
0.08	5.4936	13.4960	352.745	3.81	0.0455	62.66
0.10	5.4950	13.5040	353.113	0.27	0.0700	100.52
0.20	5.5025	13.5048	354.174	3.74	0.0921	139.19

In order to study the effect of BFO on the magnetic response of the BNT, in Figure 9 we show the magnetization curves vs. magnetic field (M–H) at room temperature (300 K) between −30 and 30 kOe. The sample doped with 5% BFO exhibits a paramagnetic behavior (Figure 9a), like pure BNT, indicating that this percentage is not enough to modify its magnetic behavior. When increasing the doping to 10% (Figure 9b), it is observed a small cycle of hysteresis characteristic of a ferrimagnetic response, with a coercive field of 152.5 kOe and a remanent magnetization of 5.63×10^{-5} emu/g. The Figure 9c shows the magnetic behavior of the system for 20% BFO; the increase in BFO enhances the magnetic response, increasing the values of both, the remanent magnetization and the magnetization at the maximum magnetic field (since none magnetic measures

were carried out until saturation, we introduce the M_{Hmax} parameter as the one corresponding to the magnetization of the sample at the maximum magnetic field. This parameter allows us to analyze the magnetic order obtained); according to the above, we get a greater magnetic order and a greater "magnetic memory" in the system. Contrary to the increase of the remanent magnetization the coercive field decreases, which can be explained by the presence of spurious phases in the BNT–xBFO.
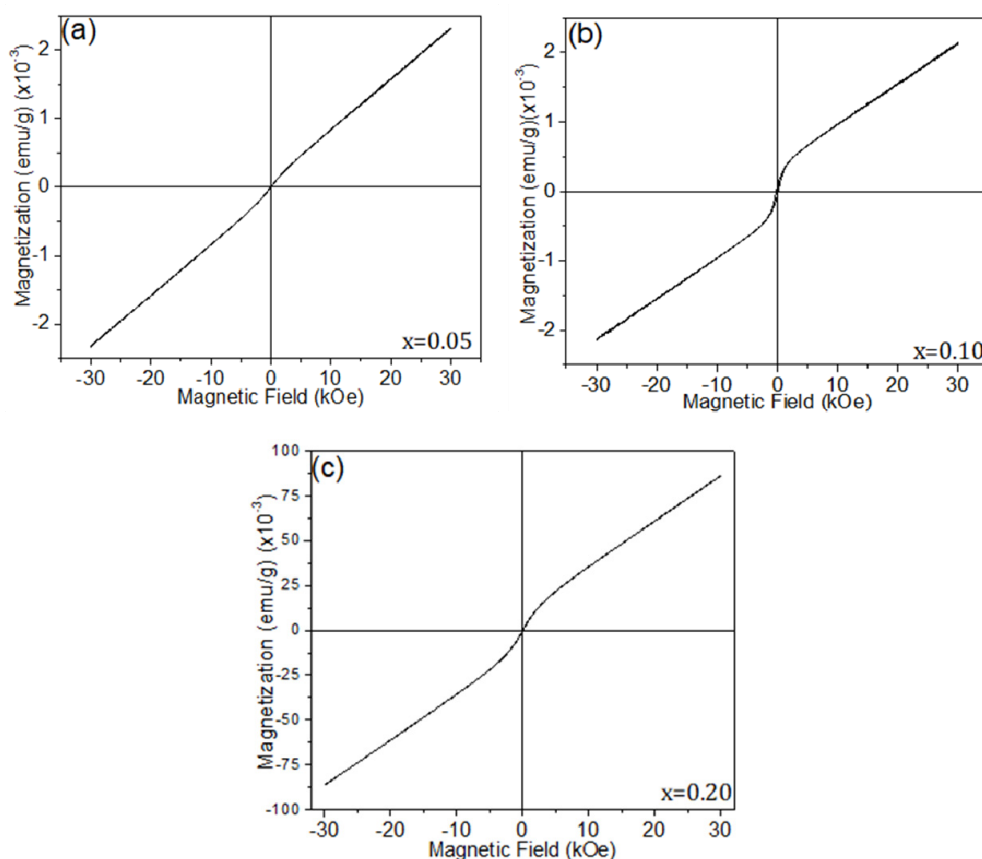

Figure 9. Magnetization curves vs. magnetic field for the BNT–xBFO system at different concentrations (a) x = 0.05, (b) x = 0.10 and (c) x = 0.20 at 300 K.

As expected, the M–H relationship for the BNT–BFO system is highly dependent on the composition. It is also expected a stronger magnetic behavior at low temperatures since the thermal randomness effect tends to break the magnetic order. To observe this behavior, the sample doped with 10% BFO was subjected to a magnetic field at 50 K, 200 K and 300 K, as is shown in the Figure 10. It is seen that both the remanent magnetization and the M_{Hmax} increase with the decrease of temperature, evidencing higher magnetic ordering and higher magnetic memory in response to decreased thermal randomness effect. However, the coercive field decrease can be explained by the "competition" between the two magnetic behaviors (paramagnetism-antiferromagnetism) that results in a weak ferrimagnetism: the concentration of BFO is not enough to provide the magnetic order that compensates the low thermal effect by decreasing the temperature; as it is known, paramagnetism is temperature dependent ($M \propto T^{-1}$): at lower T, it is easier to obtain a magnetic response for low applied fields.
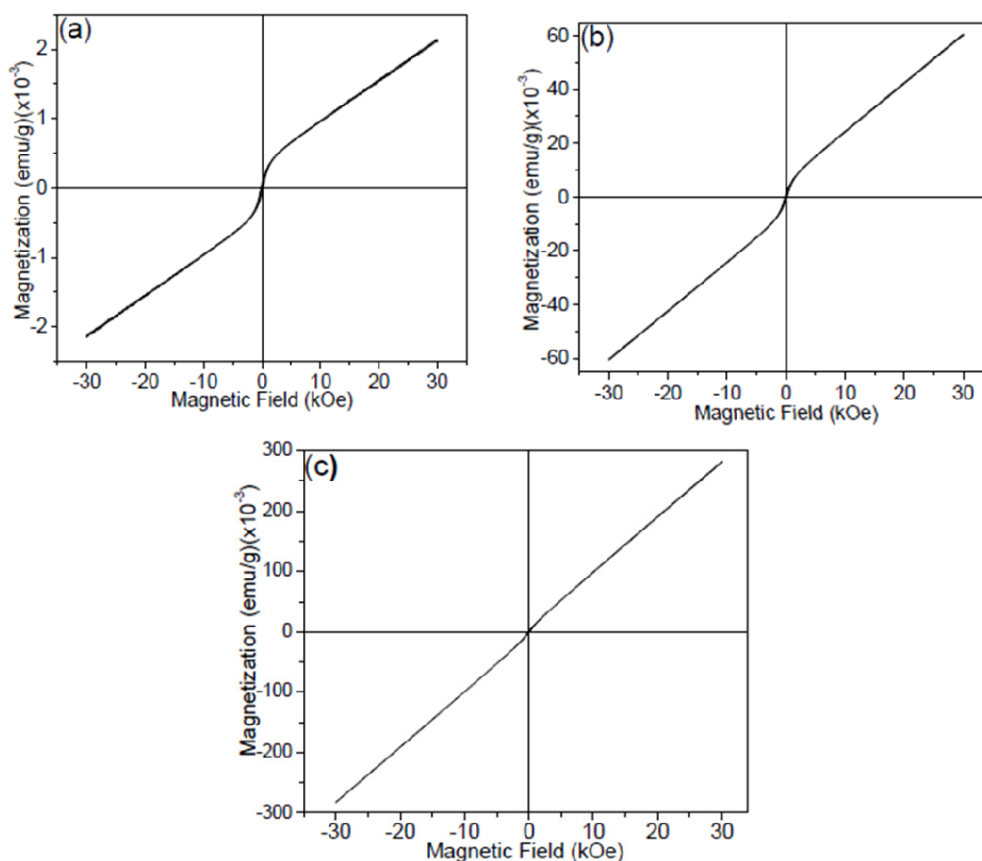
Figure 10. Magnetization curves vs. magnetic field for the BNT–xBFO system with x = 0.10 at different temperatures (a) 300 K, (b) 200 K and (c) 50 K.

Figure 11 shows the typical evolution of the dielectric permittivity versus temperature for different frequencies and for different BNT–xBFO compositions. For x = 0 two anomalies are observed in the dielectric constant: a hump around 198 °C where the dielectric constant is frequency dependent and a diffuse maximum near 326 °C, almost frequency independent, these results were consistent with previous studies [53–55]. The hump may be related to a phase coexistence, where the long-range ferroelectric domains breaking down into polar nanoregions (PNRs) at and above the T_{FD} [56]. The diffuse peak could be related to a transition from an orthorhombic non-polar phase to a tetragonal non-polar phase [57]. It has been reported an additional dielectric anomaly between 520–540 °C, although not measured in this study, associated with a phase transition from tetragonal to cubic [38]. The dependence of the dielectric constant with the frequency disappears at $T_{FD} \sim 262$ °C.
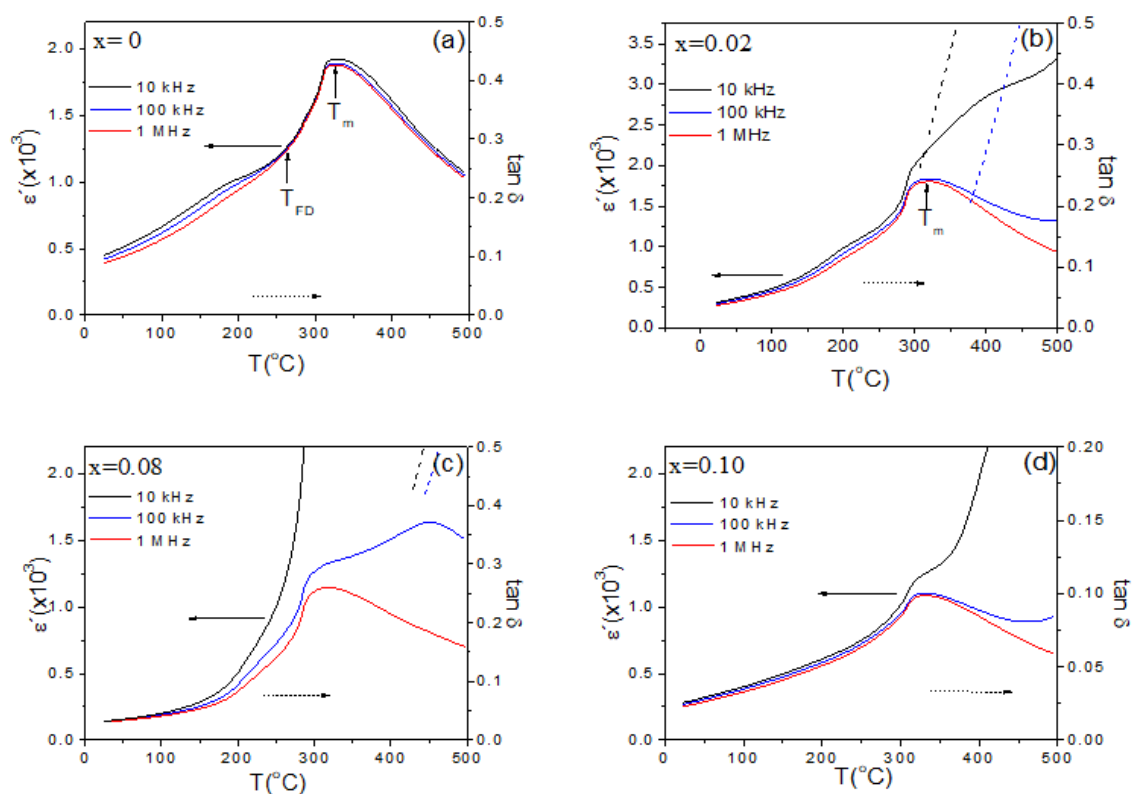
Figure 11. Temperature dependence on dielectric constant ε' and dielectric loss tanδ of BNT–xBFO ceramics measured at various frequencies. (a) x = 0.00, (b) x = 0.02, (c) x = 0.08, (d) x = 0.10.

The hump at 198 °C is only observed for pure BNT and for the lowest dopant content (x = 0.02). The sudden increase in permittivity at high temperature relates to the increase in electrical conductivity; however, it is observed that this phenomenon appears at lower temperatures as the BFO content increases. Some authors suggest that the increase in conductivity in the solid solution is related to an increase in the concentration of oxygen vacancies induced by the reduction of Fe^{3+} in Fe^{2+}, the concentration of iron increases as x increases [54]. In BNT, the abnormality of permittivity is associated with ferroelectric relaxor behavior [58]; and this type of behavior should disappear with increasing BFO content. However, the frequency-dependent anomaly, better observed in dielectric loss curves (tanδ), remains for all compositions. For x = 0, the location of a maximum around 200 °C is associated with a nonpolar phase, while the polar character drops sharply at the phase coexistence temperature. In this respect, studies carried out on the system BNT–xBFO report that for x < 0.5 the temperature at which the hump appears corresponds to the depolarization temperature [54]. It has been reported that for BFO rich compounds, the conductivity is due to oxygen vacancies and these can play a key role in the relaxation phenomenon [59]; in fact, the mechanism of relaxation linked to oxygen vacancies is present in all compositions, but its contribution increases when the amount of Fe increases.

4. Conclusions

The combustion reaction method allowed the synthesis of BNT–xBFO perovskite for all concentrations; the molecular homogeneity achieved in this method favors the formation of the desired phase. According to FTIR results, when x is increased, there is a displacement of the bands associated with the vibrations of the TiO_6 octahedron and new bands appear related to the twisting mode of the Bi–O bond and the stretching mode of the Fe–O bond. The addition of BFO to the BNT system maintains the rhombohedral symmetry and the crystallite size increases, however there is no phase transition in the compositions studied. The antiferromagnetic behavior of the BFO contributes to the magnetic order of the BNT (paramagnetic) giving place to a magnetic hysteresis loop with a ferrimagnetic response for x = 0.10. For x = 0.20; the remanent magnetization and the magnetization at the maximum magnetic field are higher, instead the coercive field is lower, as can be seen from the hysteresis magnetic loops at different temperatures. In the permittivity curves as a function of the temperature, there is an increase in conductivity due to the incorporation of iron in the crystalline structure, and it is seen a relaxor behavior for all compositions.

Acknowledgments

Conflict of interest

The authors confirm that there is not conflict of interest.

References

1. Fruth V, Mitoseriu L, Berger D, et al. (2007) Preparation and characterization of $BiFeO_3$ ceramic. *Prog Solid State Ch* 35: 193–202.
2. Chengang X, Dunmin L, Kwok KW (2008) Structure, electrical properties and depolarization temperature of $(Bi_{0.5}Na_{0.5})TiO_3$–$BaTiO_3$ lead-free piezoelectric ceramics. *Solid State Sci* 10: 934–940.
3. Hagiyev MS, Ismaizade IH, Abiyev AK (1984) Pyroelectric properties of $(Na_{1/2}Bi_{1/2})TiO_3$ ceramics. *Ferroelectrics* 56: 215–217.
4. Suchanicz J, Nowakowska-Malczyk M, Kania A, et al. (2021). Effects of electric field poling on structural, thermal, vibrational, dielectric and ferroelectric properties of $Na_{0.5}Bi_{0.5}TiO_3$ single crystals. *J Alloy Compd* 854: 157227.
5. Chen M, Xu Q, Kim BH, et al. (2008) Structure and electrical properties of $(Na_{0.5}Bi_{0.5})_{1-x}Ba_xTiO_3$ piezoelectric ceramics. *J Eur Ceram Soc* 28: 843–849.
6. Wang G, Zhongming F, Murakami S, et al. (2019) Origin of the large electrostrain in $BiFeO_3$–$BaTiO_3$ based lead-free ceramics. *J Mater Chem A* 7: 21254–21263.
7. Wang D, Wang M, Liu F (2015) Sol-gel synthesis of Nd-doped $BiFeO_3$ multiferroic and its characterization. *Ceram Int* 41: 8768–8772.
8. Li ZJ, Hou ZL, Song WL, et al. (2016) Mg-substitution for promoting magnetic and ferroelectric properties of $BiFeO_3$ multiferroic nanoparticles. *Mater Lett* 175: 207–211.

9.   Cheng S, Zhang BP, Zhao L, et al. (2019) Enhanced insulating and piezoelectric properties of $BiFeO_3$–$BaTiO_3$–$Bi_{0.5}Na_{0.5}TiO_3$ ceramics with high Curie temperature. *J Am Ceram Soc* 102: 7355–7365.

10. Dorcet V, Marchet P, Trolliard G (2007) Structural and dielectric studies of the $Na_{0.5}Bi_{0.5}TiO_3$–$BiFeO_3$ system. *J Eur Ceram Soc* 27: 4371–4374.

11. Wu J, Wang J (2009) Multiferroic behaviour and orientation dependence of lead-free $(1–x)BiFeO_3$–$x(Bi0.50Na_{0.50})TiO_3$ thin films. *J Phys D Appl Phys* 42: 195405.

12. Hieno A, Sakamoto W, Moriya M, et al. (2011) Synthesis of $BiFeO_3$–$Bi_{0.5}Na_{0.5}TiO_3$ thin films by chemical solution deposition and their properties. *Jpn J Appl Phys* 50: 09NB04.

13. Ji WJ, Chen YB, Zhang ST, et al. (2012) Microstructure and electric properties of lead-free $0.8Bi_{1/2}Na_{1/2}TiO_3$–$0.2Bi_{1/2}K_{1/2}TiO_3$ ceramics. *Ceram Int* 38: 1683–1686.

14. Kim C Y, Sekino T, Niihara K (2003) Synthesis of bismuth sodium titanate nanosized powders by solution/sol-gel process. *J Am Ceram Soc* 86: 1464–1467.

15. Ma YJ, Cho JH, Lee YH, et al. (2006) Hydrothermal synthesis of $(Bi_{1/2}Na_{1/2})TiO_3$ piezoelectric ceramics. *Mater Chem Phys* 98: 5–8.

16. Van Hal HAM, Groen WA, Maassen S, et al. (2001) Mechanochemical synthesis of $BaTiO_3$, $Bi_{0.5}Na_{0.5}TiO_3$ and $Ba_2NaNb_5O_{15}$ dielectric ceramics. *J Am Ceram Soc* 21: 1689–1692.

17. Patil KC, Aruna ST, Ekambaram S (1997) Combustion synthesis. *Curr Opin Solid St M* 2: 158–165.

18. Fityk 0.9.2 a curve fitting and data analysis program, 2010. Available from: http://www.unipress.waw.pl/fityk/.Marcin Wojdyr.

19. Larson AC, Von Dreele RB (2004) General Structure Analysis System (GSAS), Los Alamos National Laboratory Report LAUR 86-748.

20. Cullity BD, Stock SR (2001) *Elements of X-ray Diffraction*, 3 Eds., New York: Prentice Hall Publication.

21. Rietveld HM (1967) Line profiles of neutron powder-diffraction peaks for structure refinement. *Acta Crystallogr* 22: 151–152.

22. Warren BE, Averbach BL (1950) The effect of cold-work distortion on X-ray patterns. *J Appl Phys* 21: 595–599.

23. Suryanarayana C, Norton MG (1998) Part I Basics, *X-ray Diffraction: A Practical Approach*, New York: Plenum Press.

24. Xavier E (2004) Introduction to the behavior of ceramic pastes (in Spanish). Available from: https://www.scienceopen.com/document?vid=178d6249-68f8-445a-b6b6-19140255a435.

25. Moreno R (2005) Rheology of ceramic suspensions. Available from: http://boletines.secv.es/upload/20070111131337.contenido_adicional_45[1].pdf.

26. Nakamoto K (2008) *Infrared and Raman Spectra of Inorganic and Coordination Compounds: Part A: Theory and Applications in Inorganic Chemistry*, 6 Eds., John Wiley & Sons.

27. Chen Z, He X (2010) Low-temperature preparation of nanoplated bismuth titanate microspheres by a sol-gel-hydrothermal method. *J Alloy Compd* 497: 312–315.

28. Li JB, Wang H, Hou YD, et al. (2004) Low-temperature preparation of $Na_{0.5}Bi_{0.5}TiO_3$ nano whiskers by a sol-gel-hydrothermal method. *Nanotechnology* 15: 777–780.

29. Ng CY, Razak KA (2011) Properties of praseodymium-doped bismuth potassium titanate $(Bi_{0.5}K_{0.5}TiO_3)$ synthesised using the soft combustion technique. *J Alloy Compd* 509: 942–947.

30. Ardelean I, Cora S, Ioncu V (2006) Structural investigation of $CuO–Bi_2O_3–B_2O_3$ glasses by FT-IR, Raman and UV-VIS spectroscopies. *Optoelectron Adv M* 8: 1843–1847.

31. Ardelean I, Cora S, Rusu D (2008) EPR and FT-IR spectroscopic studies of $Bi_2O_3–B_2O_3–CuO$ glasses. *Physica B* 403: 3682–3685.

32. Bhushan B, Basumallick A, Bandopadhyay SK, et al. (2009) Effect of alkaline earth metal doping on thermal, optical, magnetic and dielectric properties of $BiFeO_3$ nanoparticles. *J Phys D Appl Phys* 42: 065004–065011.

33. Ramadevudu G (2011) FTIR and some physical properties of alkaline earth borate glasses containing heavy metal oxides. *Int J Eng Sci Technol* 3: 6998–7005.

34. Gurmeet L, Verma N (2014) Synthesis and characterization of $BiFeO_3$ nanowires and their applications in dye-sensitized solar cells**.** *Mat Sci Semicon Proc* 21: 206–211.

35. Chiang YM, Birnie DP, Kingery V (1997) *Physical Ceramics-Principles for Ceramic Science and Engineering*, John Wiley & Sons.

36. Karthik T, Rao TD, Srinivas A, et al. (2012) A-site cation disorder and Size variance effects on the physical properties of multiferroic $Bi_{0.9}RE_{0.1}FeO_3$ ceramics (RE = Gd^{3+}, Tb^{3+}, Dy^{3+}). arXiv:1206.5606. Available from: https://arxiv.org/abs/1206.5606.

37. Reddy R, Rao R, Viswanath R (1989) Correlation between electronegativity differences and bond energies. *J Am Chem Soc* 111: 2914–2915.

38. Jones GO, Thomas PA (2002) Investigation of the structure and phase transitions in the novel A-site substituted distorted perovskite compound $Na_{0.5}Bi_{0.5}TiO_3$. *Acta Crystallogr B* 58: 168–178.

39. Oxford Cryosystems, Crystallographica Search-Match, Version 2,1,1,1. Available from: http://www.crystallographica.co.uk.

40. Kumar MM, Srinivas A, Suryanarayana SV (2000) Structure property relations in $BiFeO_3/BaTiO_3$ solid solutions. *J Appl Phys* 87: 855–862.

41. Bhalla AS, Guo R, Roy R (2000) The perovskite structure-a review of its role in ceramic science and technology. *Mater Res Innov* 4: 3–26.

42. Kayser GP (2014) New double perovskites obtained under extreme conditions of pressure and temperature [Doctoral Dissertation]. University Complutense of Madrid, Spain.

43. Wang D, Angel RJ (2011) Octahedral tilts, symmetry-adapted displacive modes and polyhedral volume ratios in perovskite structures. *Acta Crystallogr B* 67: 302–314.

44. Rao KS, Rajulu KCV, Tilak B, et al. (2010) Effect of Ba^{2+} in BNT ceramics on dielectric and conductivity properties. *Nat Sci* 2: 357–367.

45. Lee WC, Huang CY, Tsao LK, et al. (2009) Chemical composition and tolerance factor at the morphotropic phase boundary in $(Bi_{0.5}Na_{0.5})TiO_3$-based piezoelectric ceramics. *J Eur Ceram Soc* 29: 1443–1448.

46. Ramana EV, Suryanarayana SV, Bhima ST (2010) Synthesis and magnetoelectric studies on $Na_{0.5}Bi_{0.5}TiO_3–BiFeO_3$ solid solution ceramics. *Solid State Sci* 12: 956–962.

47. Shannon RD (1976) Revised effective ionic radii and systematic studies of interatomic distances in halides and chalcogenides. *Acta Crystallogr A* 32: 751–767.

48. Shahmoradi Y, Souri D (2019) Growth of silver nanoparticles within the tellurovanadate amorphous matrix: Optical band gap and band tailing properties, beside the Williamson–Hall estimation of crystallite size and lattice strain. *Ceram Int* 5: 7857–7864.

49. Izumi F, Ikeda T (2014) *Implementation of the Williamson–Hall and Halder–Wagner Methods into RIETAN-FP*, Nagoya Institute of Technology, 3: 33–38.

50. Patle LB, Labhane PK, Huse VR, et al. (2015) Structural analysis of Cu doped TiO_2 nanoparticles using Williamson–Hall method. *IJSRSET* 1: 66–70.

51. Suryanarayana C, Norton MG (1998) Determination of crystallite size and lattice strain, *X-ray Diffraction: A Practical Approach*, New York: Plenum Press.

52. Thompson P, Cox DE, Hastings JB (1987) Rietveld refinement of Debye–Scherrer synchrotron X-ray data from Al_2O_3. *J Appl Crystallogr* 20: 79–83.

53. Ramana E, Mahajan A, Graca M, et al. (2014) Ferroelectric and magnetic properties of magnetoelectric $(Na_{0.5}Bi_{0.5})TiO_3$–$BiFeO_3$ synthesized by acetic acid assisted sol-gel method. *J Eur Ceram Soc* 34: 4201–4211.

54. Dorcet V, Marchet P, Peña O, et al. (2009) Properties of the solid solution $(1-x)Na_{0.5}Bi_{0.5}TiO_3$–$(x)BiFeO_3$. *J Magn Magn Mater* 321: 1762–1766.

55. Yao J, Ge W, Luo L, et al. (2010) Hierarchical domains in $Na_{1/2}Bi_{1/2}TiO_3$ single crystals: Ferroelectric phase transformations within the geometrical restrictions of a ferroelastic inheritance. *Appl Phys Lett* 96: 222905.

56. Lee JH, Lee GJ, Pham TL, et al. (2020) Suppression of dielectric loss at high temperature in $(Bi_{1/2}Na_{1/2})TiO_3$ ceramic by controlling A-site cation deficiency and heat treatment. *J Sens Sci Technol* 29: 7–13.

57. Dorcet V, Trolliard G, Boullay P (2008) Reinvestigation of phase transitions in $Na_{0.5}Bi_{0.5}TiO_3$ by TEM. Part I: First order rhombohedral to orthorhombic phase transition. *Chem Mater* 20: 5061–5073.

58. He H, Lu X, Li M, et al. (2020) Thermal and compositional driven relaxor ferroelectric behaviors of lead-free $Bi_{0.5}Na_{0.5}TiO_3$–$SrTiO_3$ Ceramics. *J Mater Chem C* 7: 2411–2418.

59. Li W, Chen K, Yao Y, et al. (2004) Correlation among oxygen vacancies in bismuth titanate ferroelectric ceramics. *Appl Phys Lett* 85: 4717–4719.